




In-situ thin film copper–copper thermocompression bonding for quantum cascade lasers

Sina Rouhi¹, Mehtap Ozdemir^{1,2,*} , Merve Ekmekcioglu¹, Serap Yigen¹, Yasemin Demirhan¹, Anna Szerling³, Kamil Kosiel³, Maciej Kozubal³, Renata Kruska³, Piotr Prokaryn³, Mehmet Ertugrul⁴, John L. Reno⁵, Gulnur Aygun¹, and Lutfi Ozyuzer^{1,2}

¹Department of Physics, Izmir Institute of Technology, Urla, 35430 Izmir, Turkey

²Teknoma Technological Materials Inc., Izmir Technology Development Zone, Urla, 35430 Izmir, Turkey

³Institute of Electron Technology, Al.Lotnikow 32/46, 02-668 Warszawa, Poland

⁴Department of Electric-Electronics, Ataturk University, 25030 Erzurum, Turkey

⁵Sandia National Laboratories, Department 1123, CINT, MS 0601, Albuquerque, NM 87185-0601, USA

Received: 22 February 2021

Accepted: 2 May 2021

Published online:
15 May 2021

© The Author(s), under exclusive licence to Springer Science+Business Media, LLC, part of Springer Nature 2021

ABSTRACT

The choice of metals, bonding conditions and interface purity are critical parameters for the performance of metal–metal bonding quality for quantum cascade lasers (QCLs). Here, we present a novel approach for the thermocompression bonding of Cu–Cu thin films on GaAs-based waveguides without having any oxide phase, contamination or impurities at the interface. We designed a hybrid system in which magnetron sputtering of Ta, thermal evaporation of Cu and Cu–Cu thermocompression bonding processes can be performed sequentially under high vacuum conditions. GaAs/Ta/Cu and Cu/Ta/GaAs structures were thermocompressionally bonded in our in-situ home-built bonding system by optimizing the deposition parameters and bonding conditions. The grown thin film and the obtained interfaces were characterized using x-ray diffraction (XRD), scanning electron microscopy (SEM) and energy-dispersive x-ray spectroscopy (EDX) techniques. The optimum Ta and Cu films' thicknesses were found to be about 20 nm and 500 nm, respectively. EDX analysis showed that the Ta thin film interlayer diffused into the Cu structure, providing better adhesivity and rigidity for the bonding. Additionally, no oxidation phases were detected at the interface. The best bonding quality was obtained when heated up to 430 °C with an applied pressure of 40 MPa during bonding process.

Address correspondence to E-mail: mehtapozdemir@teknoma.net

1 Introduction

Quantum cascade lasers (QCLs) are still under development as terahertz (THz) wave generation sources for a variety of functional applications [1, 2]. The major interest in this field is developing compact, coherent wave emission sources for sensing, imaging and spectroscopic applications [3, 4]. Furthermore, some detection devices like THz near field radars can detect explosive materials, toxic gases, and biological warfare and are of interest for military applications [5]. The first experimental demonstration of a QCL was produced by Bell Laboratories in 1994 and operated with a wavelength of 4.3 μm and 8 mW peak power. Originally, these lasers operated in pulsed mode at cryogenic temperatures [6, 7]. Since then, QCL technology has been greatly improved. Presently the use thermoelectrical cooling and can provide a wavelength range of 3.5–24.0 μm , between mid-infrared and far-infrared [8–15], and elevate the peak power to watt levels [16, 17]. Moreover, development of pulsed devices enabled the lasers to provide wavelength up to 16.0 μm [18]. However, cryogenic cooling is still required for longer wavelengths [19] and the maximum operating temperatures appeared to be in the range of 175–210 K for 3.0 THz emissions [20, 21].

The new generation of THz QCLs is developed-based on quantum confinement that leads to inter-subband transitions. They use a double-surface waveguide grown on GaAs substrate while emitting at 4.6 THz. The operating temperature is still a problem due to secondary phase formation at the waveguide interface which produces heat sink to maximum 4 mW in liquid-nitrogen environment [22]. Various approaches have been developed to avoid heat sink phenomena such as Cu–Cu chemical bonding by Benzocyclobutene or direct Cu–Cu thermocompression in a hybrid process with a dielectric glue connection. Deposition of Cu and ex-situ thermocompression wafer bonding is well known but the problem is oxidation of the copper layers can cause problems in the performance of the lasers. The second problem is the connection of the copper layers which are oxidized [23–25]. Elemental copper tends to oxidize even at room temperature, but bonding has to be performed above 400 °C for more inter-lattice diffusion [26, 27]. Although some of the improvements exhibited better performance of the bonded Cu–Cu interface such as self-assembled monolayer

(SAM) passivation, nevertheless a small amount of oxide still existed at metallic intersection [28].

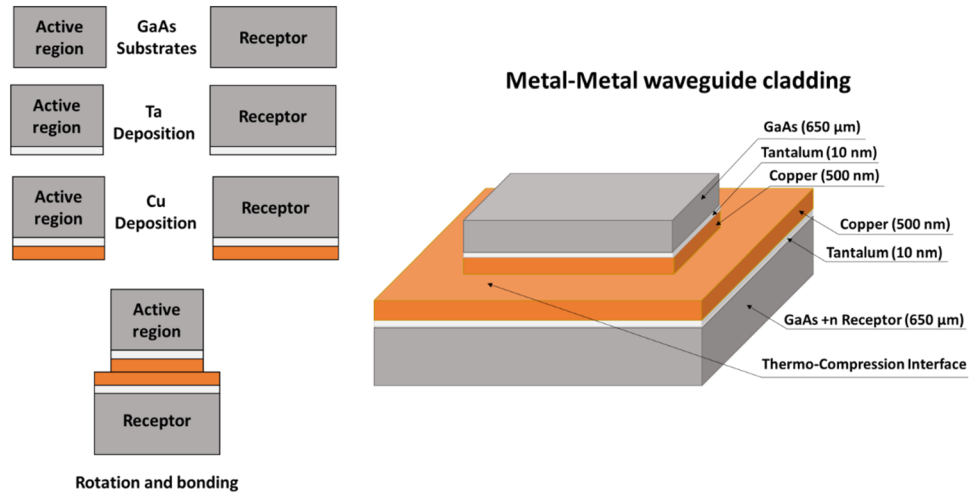
The present study reports a novel approach to avoid any oxide phase formation at the waveguides interface during Cu–Cu thermocompression bonding process. A hybrid system consisting of both magnetron sputtering and thermal evaporation was designed and combined into a single vacuum chamber along with an in-situ thermocompression bonding setup. The homemade single vacuum chamber system was equipped with heaters to apply high temperatures and mechanical compression to apply pressure during bonding. As a result, deposition of tantalum and copper thin films on wafers surfaces and thermocompression bonding of Cu–Cu interface could be performed sequentially without breaking high vacuum conditions. Excellent Cu–Cu bonding quality was achieved by means of this method without any undesired phase formation or impurities at the interface. The structural properties and elemental compositions of the interface as a result of bonding have been characterized using x-ray diffraction (XRD), scanning electron microscopy (SEM) and EDX analysis.

2 Experimental methods

Metal–metal waveguide devices for thermocompression bonding procedure were prepared as illustrated in Fig. 1. GaAs substrates were used for experiments and play the role of active region and receptor structures. In final experiments, we used THz QCLs in which active regions were deposited on GaAs substrate with thickness of about 650.0 μm and dimensions of 4-inch wafers. The THz QCLs were grown by using molecular beam epitaxial (MBE) method on pure GaAs wafer and the active region is based on 4 layers of resonant phonon discharge. This structure was repeated 207 times and the design radiation frequency is 3.6 THz. Before deposition, the active region wafer was diced into 5 mm \times 5 mm pieces which were then mounted on sample holder using silver paint.

In order to bond active region THz QCLs with the receptor and avoid any oxide phase formation during this process, a novel approach has been developed using a home-built system. The system was specifically designed to combine thin film deposition methods and thermocompression bonding process

Fig. 1 The schematic of the bonded metal–metal waveguide structure



into a single vacuum chamber. Thus, the designed single vacuum chamber system could provide step-by-step thin film deposition process, followed by thermocompression bonding without breaking high vacuum conditions. Figure 2 shows a schematic of both the internal and external components of the system. High vacuum conditions inside the main chamber were maintained by mechanical and turbomolecular pumps. The system was equipped with AC and DC power supplies to provide for thermal evaporation and magnetron sputtering, respectively. Moreover, an external apparatus was designed and connected for mechanical compression.

The physical vapor deposition (PVD) processes were initiated after reaching a vacuum lower than 5×10^{-6} Torr inside the chamber. First, a tantalum (Ta) thin film was sputtered onto both samples from a 2-inch Ta target (99.99% purity) at a DC power of 30 W (312.0 V and 80 mA) with argon (Ar) gas flow of 40 sccm, keeping the chamber pressure at $\sim 10^{-3}$ Torr. The copper (Cu) thin film was sequentially evaporated on top (at 1.2 V and 185 A of AC power) after the gas flow was stopped and a vacuum condition was established at $\sim 10^{-6}$ Torr. The copper source was a 0.3 mm thick molybdenum thermal evaporation boat with Cu shot (99.99% purity). The

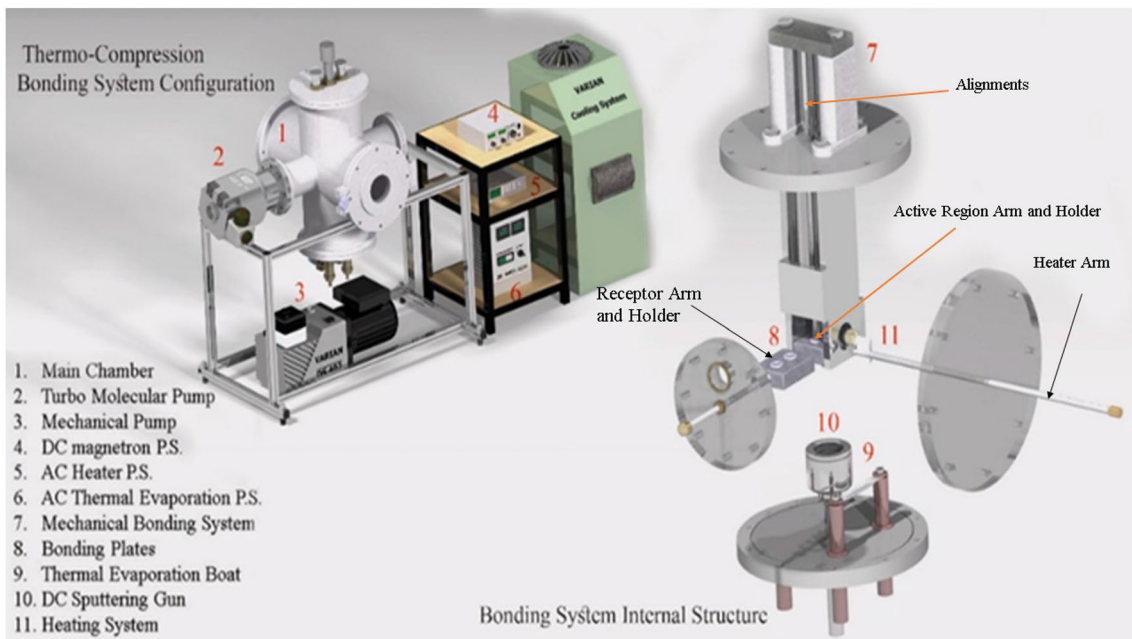


Fig. 2 The schematic of the home-built system for thermocompression bonding process showing internal and external components

sample to target and shot distances were 7 and 12 cm for Ta and Cu, respectively.

The thermocompression bonding of the Ta/Cu-coated waveguides was performed by using five externally controllable arms mounted into the deposition chamber (see Fig. 3). Two of the arms were designed to keep sample holders and the other two were employed to align samples properly during the mechanical compression process. The last one was to control the heater placement. The thermomechanical bonding process consisted of two main parts: (i) gradual heating and (ii) mechanical pressure. After Ta/Cu depositions, the THz QCL active region sample was raised, and the arm carrying the receptor sample was flipped by 180° in order to face the active region on the upper holder. Then, a gradual heating process was performed by using a quartz lamp and a resistor. The quartz lamp was placed between the samples to gradually increase the temperature. In addition, the receptor sample was heated by a resistor wire to further improve the adhesion. After achieving the optimum temperature, the quartz lamp was moved from between the samples to a position close to the samples in order to maintain the

temperature during the bonding process. The mechanical pressure was then applied after lowering the upper holder. The applied pressure was controlled by the springs located outside of the vacuum chamber and determined with respect to the sample's size. The optimum compression pressure was found as 40 MPa.

Figure 4 shows the simultaneous measurements of temperature and pressure during the bonding process. The temperature was gradually increased to the optimum processing temperature. When the thermal peak of 430°C was reached, a mechanical compression of 40 MPa was applied for bonding. After bonding process was completed, the lamp was turned off and the sample was left to cool. During the entire bonding operation, high vacuum condition (about 10^{-6} Torr) was maintained inside the chamber.

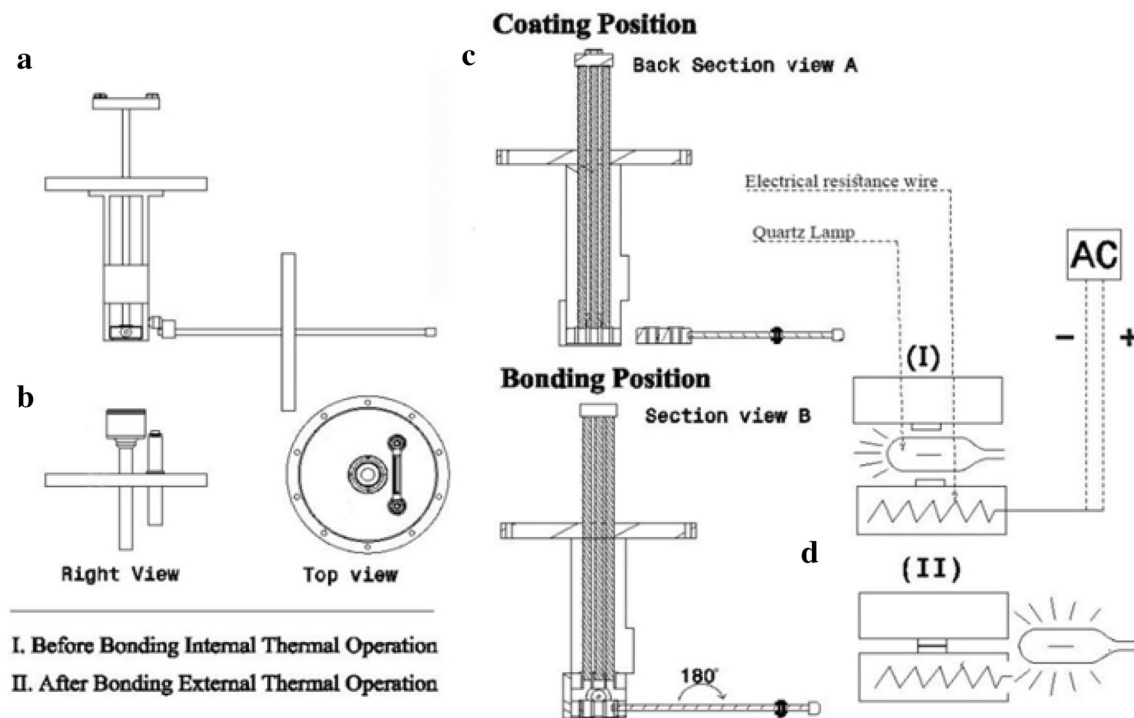


Fig. 3 The schematic of thermocompression bonding procedure. (a) The position of components before the deposition. (b) The top and right view of the system. (c) The coating and bonding

positions from different section views. (d) The positioning of quartz and resistor heaters before and after thermal operations

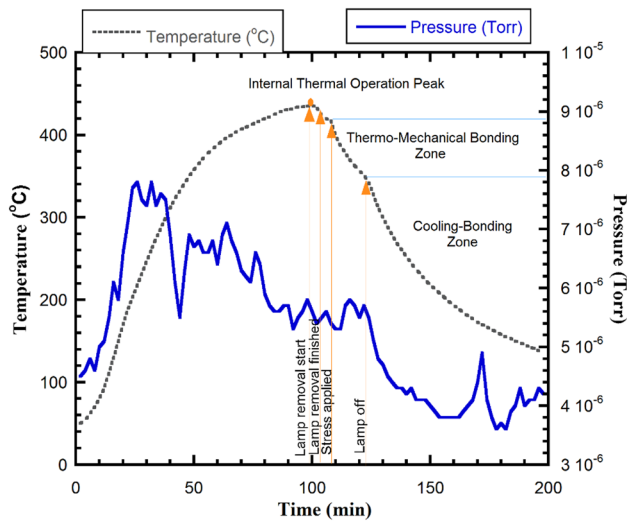


Fig. 4 Temperature and vacuum pressure profiles during thermocompression bonding operation

3 Results and discussion

3.1 Thickness optimization

Thickness of Ta and Cu thin films was optimized using surface profilometry. Figure 5(a) shows the thickness of Ta films sputtered for various deposition times. Data points were connected by lines for guide to eyes. The thickness of Cu films was optimized by evaporating different amounts of Cu shot placed in the molybdenum boat (see Fig. 5(b)). The thin film thicknesses used were around 20 nm for Ta and 500 nm for Cu. The thickness distribution over the substrate surfaces were measured by Veeco DEK-TAK150 surface profilometer for determination homogeneity of the films. The thickness variation for both Cu and Ta films are less than 1% in 5 mm × 5 mm sample size.

3.2 Characterizations of copper thin film

Scanning electron microscopy (SEM) images were taken to investigate surface morphology of Cu films evaporated on the substrates. Figure 6 shows SEM images obtained at different magnifications. SEM analysis clearly shows that thermal evaporation method could provide a smooth and uniform coating of Cu on the substrate without any sign of cracks commonly seen in DC magnetron sputtered Cu films. Microstructural features of Cu films seen from SEM images show that a homogenous distribution of

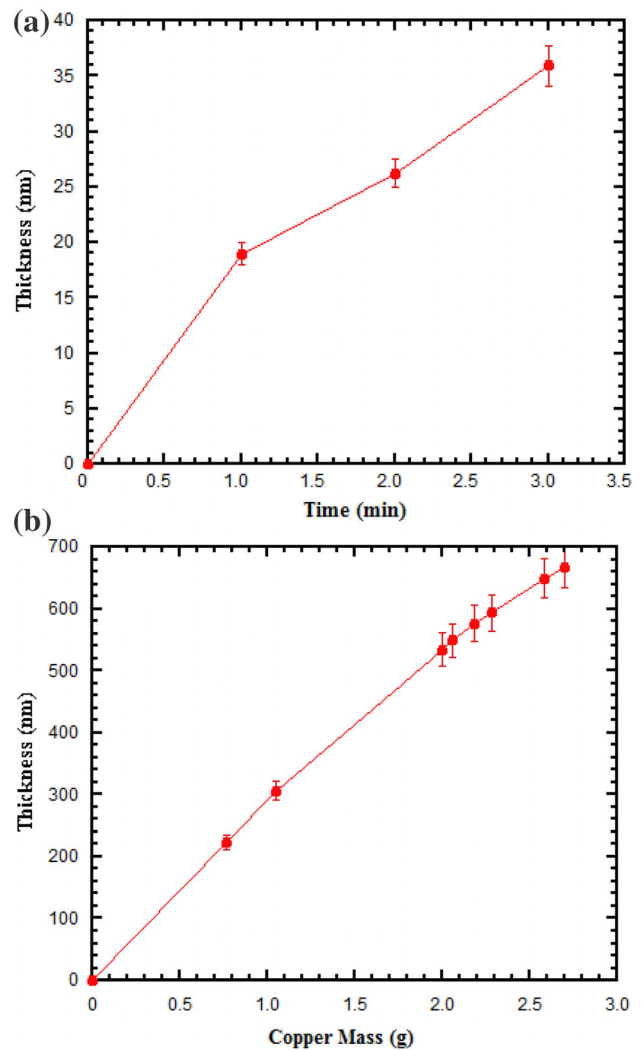


Fig. 5 Thickness of (a) Ta thin film with respect to deposition time, and (b) Cu thin film versus Cu mass evaporated

grains with similar size was observed over the surface.

Crystallographic structure of evaporated Cu films was characterized with x-ray diffraction (XRD) analysis. Figure 7 shows a XRD spectrum taken from an as-deposited Cu thin film. There are three peaks observed at diffraction angles of 43.3°, 50.5° and 74.1° that correspond to the (111), (200) and (220) crystal orientations of Cu, respectively [29, 30]. In addition, there are two small peaks appearing at around 39.0° and 46.0° that correspond to CuO [31, 32]. Since the evaporation process was performed at high vacuum conditions, the formation of CuO grains inside the deposited Cu thin film was attributed to the possible oxidation of Cu the shot used as source material for thermal evaporation. In addition, Rietveld refinement

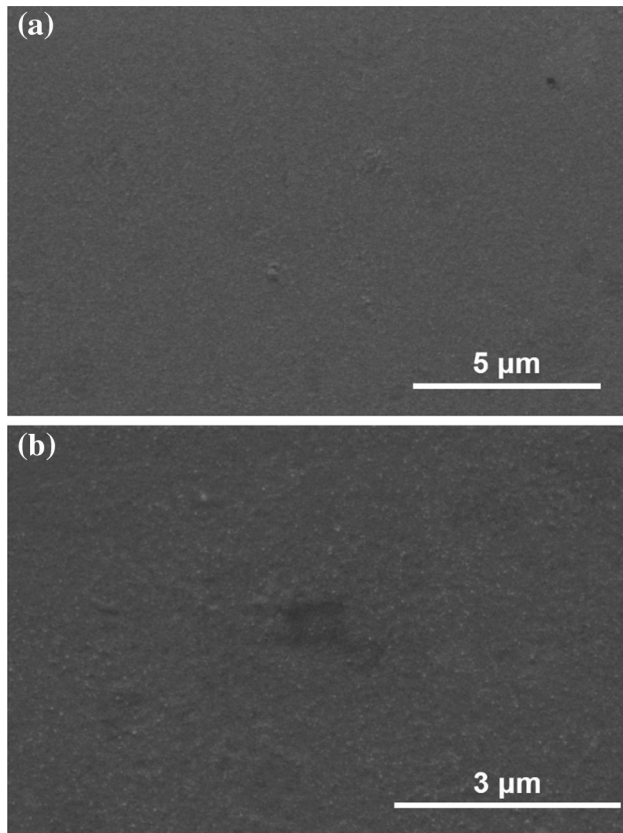


Fig. 6 SEM images of thermally evaporated Cu thin films at various magnifications. (a) 25,000 × and (b) 50,000 ×

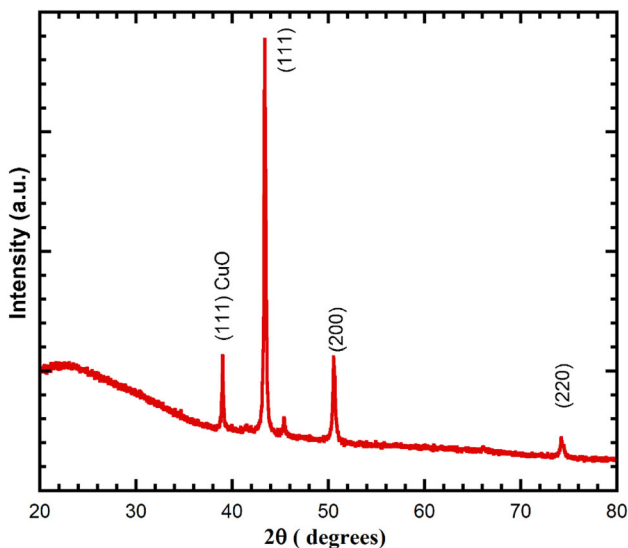


Fig. 7 XRD spectrum of thermally evaporated Cu films

was conducted on the XRD data in order to obtain crystal structure parameters (Table 1). Rietveld analysis by match software phase identification program has been carried out. At the beginning, the

experimental details are selected and introduced to program as radiation type (X-rays), wavelength (1.54 Å) and diffraction angle range. The diffraction data is imported to the program software and the candidate (potential) phases are listed (phase identification procedure has been run). The best matching phases are chosen and after selecting the matching phases, the analysis report is obtained that includes the peak list via the 2θ , d spacing, FWHM values. Both Rietveld analysis results and experimentally obtained XRD data are consistent with the reports found in literature and matches well with JCPDS card.

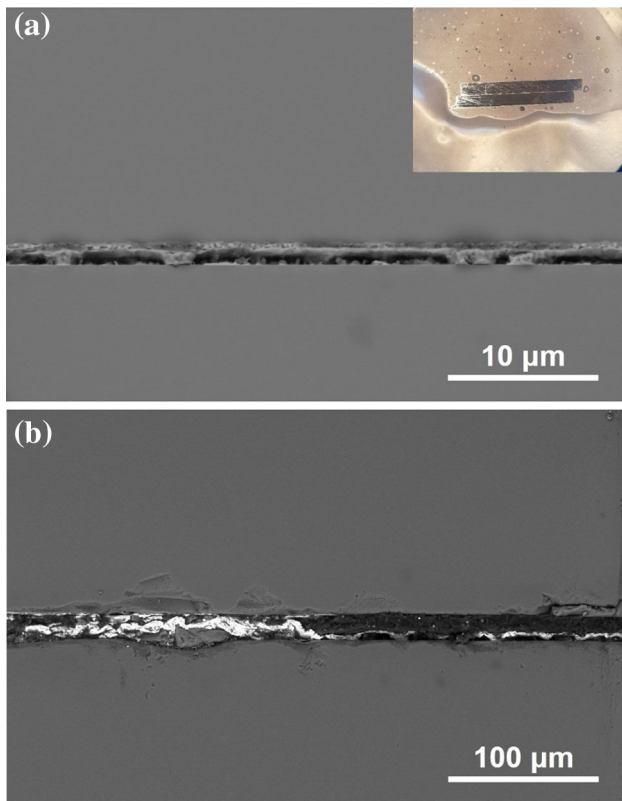
XRD analysis is a simple and powerful method to estimate crystallite size. The average crystallite size can be obtained using the Scherrer equation [33]: $D = K \lambda / \beta \cos \theta$ where K is the shape factor, λ is the X-ray wavelength, θ is the Bragg diffraction angle, and β is the full-width at half-maximum (FWHM) of the peak corresponding to θ . $K = 0.9$ was used to estimate the crystallite size D . The calculated D values are only estimates since the exact value of the constant K is unknown for the present system [34, 35]. The calculated average crystallite size of the Cu thin film for each peak is listed in Table 1. If we take the average of this results, we get 30 nm that is consistent with evaporated copper thin films found in literature [36].

3.3 Cu–Cu interface characterizations

Cu–Cu interfacial structure after the in-situ thermo-compression bonding process was investigated through cross-sectional SEM imaging. In order to obtain a good side view of the interface, the films were detached from the substrates and buried into epoxy resin. Afterwards, it was first polished with a sandpaper, followed by diamond polishing liquids with particle sizes of 9.0 μm, 3.0 μm and 1.0 μm in sequence to reveal the interface. The inset in Fig. 8(a) depicts an optical microscope image of the sample in the epoxy resin which demonstrates a clear side view obtained after the polishing process. Figure 8(a) shows a cross-sectional SEM image of a well-bonded interface where a clean connection of Cu films can be seen. Figure 8(b) displays a SEM image of a poorly bonded interface for comparison. It clearly exhibits the deformations and cracks along the interface. This deformity was probably formed during the mechanical compression process. The epoxy

Table 1 Rietveld refinement results for the thermally evaporated Cu films

| Position [2θ] | Height [cts] | FWHM [2θ] | d spacing [\AA] | Rel. Int. [%] | Crystallite size [nm] |
|------------------------|--------------|--------------------|----------------------------|---------------|-----------------------|
| 38.96 | 3144.06 | 0.19 | 2.31 | 25.30 | 44 |
| 43.38 | 14,402.05 | 0.26 | 2.09 | 99.38 | 33 |
| 50.53 | 4247.90 | 0.37 | 1.80 | 24.86 | 24 |
| 74.32 | 411.75 | 0.49 | 1.28 | 5.62 | 20 |

**Fig. 8** Cross-sectional SEM images of Cu–Cu interface taken from (a) a well-bonded sample, inset: optical image of the sample buried in epoxy resin and (b) a poorly bonded sample

resin filling the cracks and voids at the interface is visible in the SEM image. Interfacial analysis of the SEM images exhibits the preoccupation of forming a thin Matano interface between Cu and Cu layers that is responsible for mechanical cohesion [37]. On the other hand, nucleation of dislocations on grain boundaries is responsible for small-scale molecular motion between layers [38–40].

Energy-dispersive x-ray spectroscopy (EDX) measurements was performed on various parts of the cross-section to analyze the elemental composition around the interface. Figure 9(a) displays the six spots from which the EDX spectra were acquired. Figure 9(b) shows an example EDX spectrum taken from the bonding point marked as Spectrum 5.

Atomic weight percentage values obtained from EDX analysis for all six positions are given in Table 2.

As expected, Ga and As elements were observed without Cu and Ta from the EDX analysis performed on the sites away from the interface (Spectrum 2 and 3). Spectrum 1, taken from the spot closer to the interface, shows Ta and Cu elements' presence. Ga, As, Cu and a small amount of Ta were found around the interface and bonding point. No traces of oxidation were observed at any of these locations. EDX results confirmed the diffusion of Ta atoms into Cu structure. This improves the Ta/Cu interfacial cohesion. It is known that Ta particles can diffuse into grain boundaries of Cu film, forming a thermally and structurally more stable Ta/Cu alloy. Stabilization of Cu grain boundaries by the diffusion of Ta nanoparticles is explained by the Zener pinning effect [38]. In addition, no impurities nor oxidation appeared at the Cu–Cu bonding interface. This proves that our proposed thermocompression bonding method prevented any phase formation at the interface. Since having lower waveguide losses and higher operating temperatures compared to Ti/Pt-based metal stacks [41–43], Ta/Cu-based metal claddings would be more suitable for THz QCL applications.

4 Conclusion

We presented a novel approach for the thermocompression of Cu–Cu thin films on GaAs substrates which results in a stronger bonding without any oxide formation at the interface. We designed a hybrid system consisting of a magnetron sputtering, thermal evaporation and thermocompression bonding systems in a single vacuum chamber. This special design enables the performance of these three operations in sequence without breaking vacuum conditions. Moreover, as a result of the unique combined system, no contamination, oxidation or impurities appear at the bonding interface. In order to test the

Fig. 9 EDX analysis was performed for various sites. (a) Cross-sectional images showing the regions where EDX spectra were obtained. (b) EDX spectrum taken from the bonding point

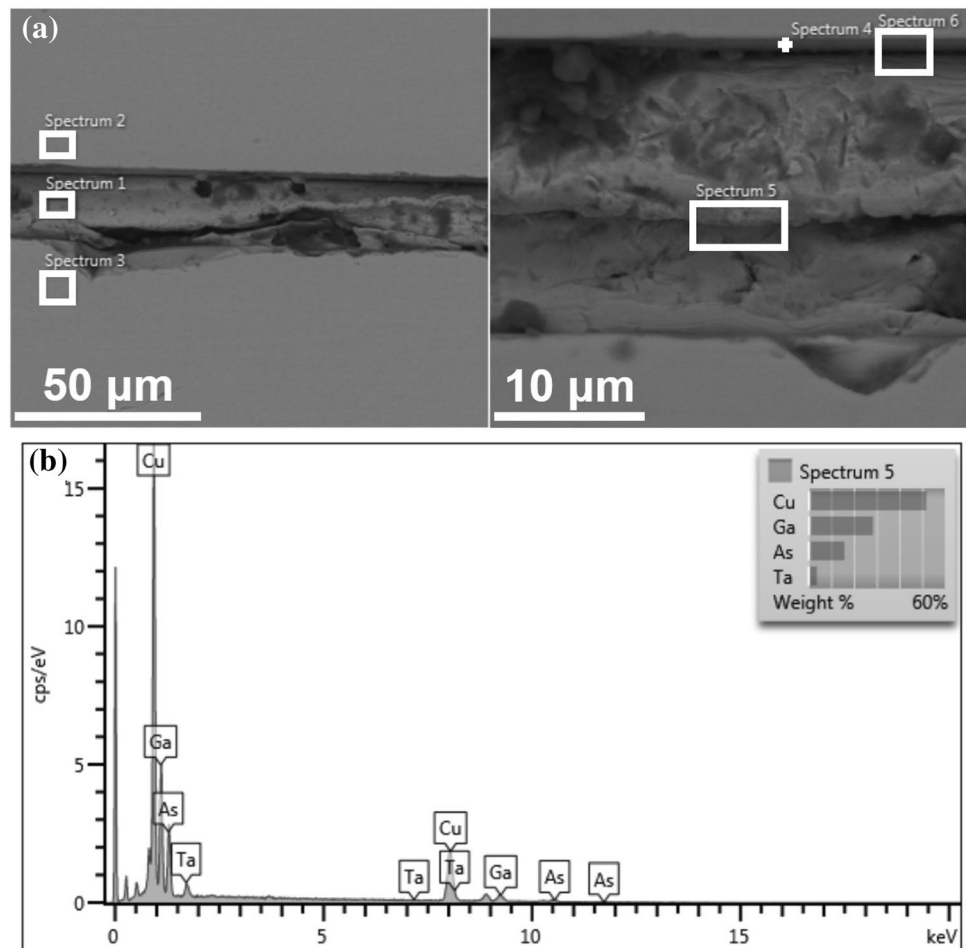


Table 2 Atomic weight percentage of the elements obtained from EDX analysis

| Weight % | Ga | As | Ta | Cu | Total |
|-------------|-------|-------|-------|-------|-------|
| Spectrum #1 | 48.99 | 0 | 10.34 | 40.67 | 100 |
| Spectrum #2 | 49.80 | 50.20 | 0 | 0 | 100 |
| Spectrum #3 | 49.99 | 50.01 | 0 | 0 | 100 |
| Spectrum #4 | 41.95 | 39.12 | 3.20 | 15.73 | 100 |
| Spectrum #5 | 28.41 | 15.96 | 3.77 | 51.86 | 100 |
| Spectrum #6 | 44.57 | 41.29 | 2.65 | 11.56 | 100 |

bonding quality of our homebuilt system, we fabricated GaAs/AlGaAs-based waveguide devices. The active region and receptor sides of the waveguides were first coated with a thin layer of sputtered Ta film, and then Cu was thermally evaporated on top. Cu-coated surfaces were initially brought face-to-face by means of externally controlled arms, and then gradually heated to high temperatures. The last step

was an application of mechanical pressure, applied externally, to initiate bonding. The thickness of the deposited thin films, the deposition parameters and the bonding conditions (temperature and pressure) were optimized to achieve the best bonding quality. Interfacial and structural characterization was performed on thin films, grown by this unique growth chamber, using x-ray diffraction (XRD), scanning electron microscopy (SEM) and energy-dispersive x-ray spectroscopy (EDX) techniques. Optimum thicknesses were 20 nm and 500 nm for Ta and Cu, respectively. EDX analysis showed that Ta thin film was diffused into Cu structure, improving the strength and cohesion of Ta/Cu. In addition, no oxidation phase was detected at the interface. The best bonding quality was obtained at 430 °C under the mechanical pressure of 40 MPa. Therefore, the proposed approach for the step-by-step fabrication with this unique system and metal–metal bonding of waveguides could be applied in the manufacturing

process of commercial QCLs to improve their lasing performance.

Acknowledgements

This research is partially supported by “Scientific and Technical Research Council of Turkey (TUBITAK)” with project number 215E113 and “The National Centre for Research and Development of Poland” (bilateral cooperation, project No. 1/POLTUR-1/2016). QCL active region grown on GaAs substrates were provided by Sandia National Laboratories (USA) supported under CINT project number #2016BU0054. We would like to thank the Research and Application Center for Quantum Technologies (RACQUT) of IZTECH for experimental facilities.

References

- C. Peng, H. Zhou, L. Zhu, T. Chen, L. Du, Y. Zhu, Y. Zou, Q. Peng, G. Chen, Z. Li, I.E.E.E. Photon, Technol. Lett. **30**, 1099 (2018)
- P. Corrigan, R. Martini, E.A. Whittaker, C. Bethea, Opt. Express **17**, 4355 (2009)
- A.Y. Pawar, D.D. Sonawane, K.B. Erande, D.V. Derle, Drug Invent. Today **5**, 157 (2013)
- L. Ozyuzer, Y. Simsek, H. Koseoglu, F. Turkoglu, C. Kurter, U. Welp, A.E. Koshelev, K.E. Gray, W.K. Kwok, T. Yamamoto, Supercond. Sci. Technol. **22**, 114009 (2009)
- Y. Demirhan, H. Alaboz, M.A. Nebioğlu, B. Mulla, M. Akkaya, H. Altan, C. Sabah, L. Ozyuzer, Supercond. Sci. Technol. **30**, 074006 (2017)
- J. Faist, F. Capasso, C. Sirtori, D.L. Sivco, A.L. Hutchinson, M.S. Hybertsen, A.Y. Cho, Phys. Rev. Lett. **76**, 411 (1996)
- Y. Guo, F.Q. Liu, J.Q. Liu, C.M. Li, Z.G. Wang, Semicond. Sci. Technol. **20**, 844 (2005)
- N. Bandyopadhyay, Y. Bai, S. Tsao, S. Nida, S. Slivken, M. Razeghi, Appl. Phys. Lett. **101**, 241110 (2012)
- R. Colombelli, F. Capasso, C. Gmachl, A.L. Hutchinson, D.L. Sivco, A. Tredicucci, M.C. Wanke, A.M. Sergent, A.Y. Cho, Appl. Phys. Lett. **78**, 2620 (2001)
- K. Kosiel, M. Bugajski, A. Szerling, J. Kubacka-Traczyk, P. Karbownik, E. Pruszyńska-Karbownik, J. Muszalski, A. Łaszcz, P. Romanowski, M. Wasiak, W. Nakwaski, I. Makarowa, P. Perlin, Photon. Lett. Polond **1**, 16 (2009)
- K. Kosiel, A. Szerling, J. Kubacka-Traczyk, P. Karbownik, E. Pruszyńska-Karbownik, M. Bugajski, Acta Phys. Pol. A **116**, 5 (2009)
- K. Kosiel, A. Szerling, M. Bugajski, P. Karbownik, J. Kubacka-Traczyk, I. Sankowska, E. Pruszyńska-Karbownik, A. Trajnerowicz, A. Wójcik-Jedlińska, M. Wasiak, D. Pierścińska, K. Pierściński, S. Adhi, T. Ochalski, G. Huyet, *Terahertz and Mid Infrared Radiation* (Springer, Dordrecht, 2011), pp. 91–100
- K. Kosiel, J. Kubacka-Traczyk, I. Sankowska, A. Szerling, P. Gutowski, M. Bugajski, Opto-Electron. Rev. **20**, 239 (2012)
- A. Szerling, R. Kruszka, K. Kosiel, M. Wzorek, K. Gołaszewska, A. Trajnerowicz, P. Karbownik, M. Kuc, T.G. Czystanowski, M.J. Walczakowski, N. Pałka, J. Nanophoton. **11**, 026004 (2017)
- A. Szerling, S. Slivken, M. Razeghi, Opto-Electron. Rev. **25**, 205 (2017)
- N. Bandyopadhyay, S. Slivken, Y. Bai, M. Razeghi, Appl. Phys. Lett. **100**, 212104 (2012)
- A. Lyakh, C. Pflügl, L. Diehl, Q.J. Wang, C. Federico, X.J. Wang, J.Y. Fan, T. Tanbun-Ek, R. Maulini, A. Tsekoun, R. Go, C. Kumar, N. Patel, Appl. Phys. Lett. **92**, 111110 (2008)
- D. Hofstetter, M. Beck, T. Aellen, J. Faist, U. Oesterle, M. Illegems, E. Gini, H. Melchior, Appl. Phys. Lett. **78**, 1964 (2001)
- Q.Y. Lu, N. Bandyopadhyay, S. Slivken, Y. Bai, M. Razeghi, Appl. Phys. Lett. **104**, 221105 (2014)
- L. Gao, J.L. Reno, S. Kumar, Photonics. **7**, 7 (2020)
- M. Franckić, L. Bosco, E. Mavrona, A. Wacker, J. Faist, *44th International Conference on Infrared, Millimeter, and Terahertz Waves (IRMMW-THz)* (IEEE, Paris, France, 2019), pp. 1–1
- Q. Hu, B.S. Williams, S. Kumar, H. Callebaut, S. Kohen, J.L. Reno, Semicond. Sci. Technol. **20**, 228 (2005)
- A. Szerling, K. Kosiel, P. Prokaryn, R. Kruszka, J. Ratajczak, K. Gołaszewska-Malec, M. Sakowicz, Z. Wasilewski, M. Szymański, M. Kuc, T. Czystanowski, M.Ö. Köklü, G. Aygün, L. Özyüzer, N. Pałka, *Quantum Sensing and Nano Electronics and Photonics XVI* (SPIE OPTO, San Francisco, 2019), p. 109261I
- A. Szerling, K. Kosiel, M. Szymanski, Z. Wasilewski, K. Gołaszewska, A. Łaszcz, M. Pluska, A. Trajnerowicz, M. Sakowicz, M. Walczakowski, N. Pałka, R. Jakiela, A. Piotrowska, J. Nanophoton. **9**, 093079 (2015)
- A. Szerling, K. Kosiel, P. Prokaryn, M. Szymański, A. Trajnerowicz, M. Sakowicz, P. Karbownik, M. Pluska, M. Walczakowski, N. Pałka, *THz for CBRN and Explosives Detection and Diagnosis* (Springer, Dordrecht, 2017), pp. 145–149
- F. Turkoglu, H. Koseoglu, S. Zeybek, M. Ozdemir, G. Aygun, L. Ozyuzer, J. Appl. Phys. **123**, 165104 (2018)
- E.J. Jang, J.W. Kim, B. Kim, T. Matthias, Y.B. Park, Met. Mater. Int. **17**, 105 (2011)

28. L. Peng, H.Y. Li, D.F. Lim, S. Gao, C.S. Tan, *61st Electronic Components and Technology Conference (ECTC)* (IEEE, Lake Buena Vista, FL, USA, 2011), pp. 22–26
29. Y. Peng, Y. Deng, Y. Wang, S. Shen, *Thin Solid Films* **616**, 562 (2016)
30. J.H. Boo, M.J. Jung, H.K. Park, K.H. Nam, J.G. Han, *Surf. Coat. Technol.* **188**, 189 (2004)
31. A.P. Moura, L.S. Cavalcante, J.C. Sczancoski, D.G. Stroppa, E.C. Paris, A.J. Ramirez, J.A. Varela, E. Longo, *Adv. Powder Technol.* **21**, 197 (2010)
32. Y. Yang, D. Xu, Q. Wu, P. Diao, *Sci. Rep.* **6**, 35158 (2016)
33. P. Scherrer, *Nachr. Ges. Wiss. Gött.* **26**, 98 (1918)
34. J.I. Langford, A.J.C. Wilson, *J. Appl. Crystallogr.* **11**, 102 (1978)
35. V. Uvarov, I. Popov, *Mater. Charact.* **85**, 111 (2013)
36. B. Giroire, M. Ali Ahmad, G. Aubert, L. Teule-Gay, D. Michau, J.J. Watkins, C. Aymonier, A. Poulon-Quintin, *Thin Solid Films* **643**, 53 (2017)
37. M.A. Dayananda, Y.H. Sohn, *Metall. Mater. Trans. A* **27**, 2504 (1996)
38. T. Frolov, K.A. Darling, L.J. Kecskes, Y. Mishin, *Acta Mater.* **60**, 2158 (2012)
39. D.F. Bahr, G. Vasquez, *J. Mater. Res.* **20**, 1947 (2005)
40. S.Y. Lee, N. Mettlach, N. Nguyen, Y.M. Sun, J.M. White, *Appl. Surf. Sci.* **206**, 102 (2011)
41. S. Fatholouloumi, E. Dupont, S.G. Razavipour, S.R. Laframboise, G. Parent, Z. Wasilewski, H.C. Liu, D. Ban, *Semicond. Sci. Technol.* **26**, 105021 (2011)
42. M. Szymański, A. Szerling, K. Kosiel, *Opt. Quantum Electron.* **47**, 843 (2015)
43. M. Szymański, A. Szerling, K. Kosiel, M. Płuska, *J. Phys. D* **49**, 275102 (2016)

Publisher's Note Springer Nature remains neutral with regard to jurisdictional claims in published maps and institutional affiliations.